Journal of Thermal Analysis and Calorimetry (2019) 138:2555–2563
https://doi.org/10.1007/s10973-019-08489-x

Nanocomposite phase change materials based on NaCl–$CaCl_2$ and mesoporous silica

Raul-Augustin Mitran[1] · **Simona Petrescu**[1] · **Simona Şomăcescu**[1] · **Oana Cătălina Mocioiu**[1] · **Lucian Buhălţeanu**[2] · **Daniela Berger**[3] · **Cristian Matei**[3]

Received: 3 December 2018 / Accepted: 10 June 2019 / Published online: 20 June 2019

Abstract

The synthesis of phase change materials based on NaCl–$CaCl_2$ molten salt mixture and mesoporous silica was investigated. The influence of mesoporous silica porosity and salt concentration on the thermal energy storage properties of the resulting materials is discussed. The nanocomposite samples were characterized by X-ray diffraction, differential scanning calorimetry, infrared spectroscopy, thermogravimetry, scanning electron microscopy and X-ray photoelectron spectroscopy. The mesoporous silica was found to act as a reactive matrix for the molten salts. Composite samples with up 95% wt. salt can be obtained and used as shape-stabilized phase change materials. The materials have heat of fusion values of up to 60.8 J g^{-1} and specific heat capacity between 1.0 and 1.1 J g^{-1} K^{-1}. The samples exhibit thermal stability up to 700 °C and can be used for high-temperature thermal energy storage through both latent and sensible heat storage mechanisms.

Keywords Mesoporous silica · Phase change materials · Molten salts · NaCl–$CaCl_2$ · Thermal energy storage

Introduction

High-temperature heat storage is becoming increasingly relevant in the areas of solar energy storage and waste heat reutilization [1–3]. Sensible and thermochemical heat storage are the main focus of current research [4, 5]. In contrast, latent heat storage for high-temperature applications has received less attention [6], even though phase change materials (PCMs) are commonly employed for low and medium temperature applications [7–11]. Molten salts, hydroxides or metals can be employed as the active heat storage phase for temperatures above 200 °C [12]. Such materials can also be used as part of hybrid heat storage systems, combining latent with sensible heat storage [6]. All high-temperature PCMs have some drawbacks, such as high change in volume during phase transition and corrosiveness for molten salts or low enthalpies and resistance to oxidation for metals [2]. In the case of low-temperature materials, shape-stabilized PCMs (ss-PCMs) are an attractive option to remove the drawbacks associated with volume change, leakage and corrosiveness, [13] since these materials retain their macroscopic solid shape even after the melting of the active PCM. Shape-stabilized PCMs can be obtained through encapsulation into an inter shell or impregnation into a high porosity matrix.

Mesoporous silica nanomaterials (MSNs) are promising matrices for the synthesis of shape-stabilized PCMs [14–16]. MSN offers high porosity, high chemical and thermal stability and an easy way to modify their properties through chemical synthesis [17, 18]. So far, only one study has considered the possibility of employing MSN for obtaining medium and high-temperature shape-stabilized heat storage composites. $LiNO_3$ and Na_2SO_4 molten salts were impregnated into a mesoporous silica material with disordered, radial pore and the resulting composites

---

Electronic supplementary material The online version of this article (https://doi.org/10.1007/s10973-019-08489-x) contains supplementary material, which is available to authorized users.

✉ Raul-Augustin Mitran
raul.mitran@gmail.com

[1] "Ilie Murgulescu" Institute of Physical Chemistry, Romanian Academy, 202 Splaiul Indepedentei, 060021 Bucharest, Romania

[2] SARA Pharm Solutions, 266-268 Calea Rahovei, 050912 Bucharest, Romania

[3] Faculty of Applied Chemistry and Material Science, University "Politehnica" of Bucharest, 1-7 Polizu Street, 011061 Bucharest, Romania

showed good heat storage properties [19]. However, no study to date was performed on the possibility of using molten salt mixtures for obtaining mesoporous silica PCM composites. One of the main advantages of MSN, the existence of an ordered mesopore array, was also not investigated to date.

We have studied the possibility of obtaining shape-stabilized PCMs using 48% NaCl–52% $CaCl_2$ (molar) mixture and two types of mesoporous silica with cubic mesopore arrangement for the first time. The salt mixture was chosen based on the reported eutectic composition of the system [2]. Shape-stabilized phase change materials were synthesized even at high salt fractions, of up to 95 mass%. The composite PCMs structure, chemical composition, surface properties and morphology were characterized. The heat storage capacity was assessed by determining the heat of fusion and specific heat capacity, while thermal stability was assessed through thermogravimetric measurements.

Experimental

Materials

Tetraethyl orthosilicate (TEOS, Fluka), HCl 37% (Sigma-Aldrich), Pluronic P123, average molar mass 5800 (Sigma-Aldrich), sodium polyacrylate, average molar mass 1600 (Sigma-Aldrich) and toluene (Sigma-Aldrich) were used as received, without further purification. NaCl (Sigma-Aldrich) and $CaCl_2$ (Sigma-Aldrich) were grounded with a mortar and pestle and dried for 4 h at 250 °C prior to use. Ultrapure water (Millipore Direct Q3 UV with Biopack UF cartridge) was used for all experiments.

Mesoporous silica synthesis

Two MSN matrices were obtained using a modification of our previously reported method [20]. Pluronic P-123 was dissolved in water and concentrated HCl, at room temperature. Next, the sodium polyacrylate or toluene pore expanders were added, followed by TEOS. The reaction mixture was stirred for 24 h at 40 °C, and then, it was transferred to an autoclave and aged at 100 °C for 24 h. The resulting white solid was filtered off, washed with water and ethanol and calcined at 550 °C for 5 h in air. The "*MSN-A*" sample was obtained using polyacrylic acid as pore expander and a molar ratio TEOS: Pluronic-P123: sodium polyacrylate: HCl: H_2O = 1: 0.016: 0.016: 6.2: 185, while the "*MSN-B*" matrix was synthesized using toluene, at a molar ratio of TEOS: Pluronic-P123: sodium polyacrylate: HCl:H_2O = 1: 0.016: 0.3: 6.2: 185.

NaCl–$CaCl_2$ shape-stabilized PCMs

The NaCl and $CaCl_2$ salts were dried at 250 °C for 4 h in an oven prior to use. A near equimolar mixture containing 48% mol NaCl and 52% mol $CaCl_2$ was prepared by quickly weighting the dried salts followed by manual mixing with a mortar and pestle for 20 min. The resulting mixture was stored in an oven at 150 °C. Shape-stabilized composites were prepared at various mass ratio by adding the NaCl–$CaCl_2$ salt and 0.5 cm^3 water to the silica matrix, in a crucible. The samples were first dried at 120 °C for 1 h in an oven, followed by treatment at 550 °C for 4 h. The resulting materials are denoted "xNaCl–$CaCl_2$/MSN," where x denotes the salt mass percent. For example, 70NaCl–$CaCl_2$/MSN-A was prepared from 166 mg NaCl–$CaCl_2$ salt mixture, 0.5 cm^3 water and 70 mg MSN-A.

Characterization

Powder X-ray diffraction (XRD) was carried out using a Bruker D8 Discover diffractometer with CuKα radiation. Nitrogen adsorption–desorption isotherms were recorded with a Quantachrome Autosorb iQ2 porosimeter at 77 K. The specific surface area was calculated with the Brunauer–Emmett–Teller (BET) theory on the 0.1–0.3 relative pressure range, while total pore volume was determined at 0.95 relative pressure (pore diameters of up to 40 nm). The pore size distribution was computed using the Barret–Joyner–Halenda (BJH) method from the desorption branch of the isotherm. A FEI Tecnai G2-F30 high-resolution electron transmission microscope equipped with a field emission electron gun was used to record transmission electron microscope (TEM) images at a maximum voltage of 300 kV. Differential scanning calorimetry (DSC) measurements were performed using a Mettler Toledo DSC 823e calorimeter under 80 $cm^3\ min^{-1}$ nitrogen flow. Samples were measured in aluminum pans with crimped, non-pierced lids. The samples were heated between 25 and 580 °C with a heating rate of 10 °C min^{-1}, followed by cooling between 580 and 100 °C with a cooling rate of 10 °C min^{-1}. All samples were dried at 150 °C prior to analysis, and the pans were weighted before and after analysis to quantify the physisorbed water. The calorimeter was calibrated with In (purity $>$ 99.999%) and Zn (purity $>$ 99.999%). The specific heat capacity (c_p) was determined by the sapphire method. The samples were held at 530 °C for 5 min, heated between 530 and 580 °C with 10°C min^{-1} and held isothermally at 580 °C for 5 min. For each c_p measurement, an empty pan, a weighted sapphire standard and the sample were analyzed. Care was taken to ensure identical experimental conditions (heating program, nitrogen flow, same pan etc.). Each c_p determination was performed in triplicate. Surface analysis performed by

X-ray photoelectron spectroscopy (XPS) was carried out on PHI Quantera equipment with a base pressure in the analysis chamber of 10^{-9} Torr. The X-ray source was monochromatized Al Kα radiation (1486.6 eV) and the overall energy resolution is estimated at 0.6 eV by the full width at half-maximum (FWHM) of the Au4f7/2 photoelectron line (84 eV). The spectra were calibrated using the C1 s line (BE = 284.8 eV) of the adsorbed hydrocarbon on the sample surface (C–C or (CH)n bonding). Fourier-transform infrared spectroscopy (FT-IR) was performed using a Nicolet 6700 spectrometer. Samples were prepared as KBr pellets. Thermogravimetric analyses were carried out using a Mettler Toledo TGA/SDTA851e thermogravimeter, open alumina pans, between 25 and 850 °C with a heating rate of 20 °C min^{-1} under synthetic air flow (80 cm^3 min^{-1}) and without further drying of the samples.

Results and discussion

Characterization of mesoporous silica

Small-angle X-ray diffraction was used to characterize the mesopore array of both matrices. At least 3 diffraction peaks could be noticed for both samples (Fig. 1a), indexed as the (111), (220) and (311) reflections of the *Fm3m* face-centered cubic space group [21]. *Fm3m* cubic silica consists of “ink-bottle” mesopores, which have a larger cavity and smaller entrances. *MSN-A* exhibits higher order Bragg reflections, indicating it has a better defined cubic mesostructure than *MSN-B*. The unit cell parameters computed from the diffraction data decrease from 22.2 nm for *MSN-A* to 19.5 nm for *MSN-B*. The silica matrices do not present wide-angle diffraction peaks, as expected from amorphous materials.

The nitrogen adsorption–desorption isotherms (Fig. 1b) are of type IV with hysteresis, denoting the mesoporous nature of the samples. *MSN-A* presents a narrower hysteresis loop than *MSN-B*, indicating better mesopore monodispersity. The same can be evidenced from the pore size distribution (Fig. 1 inset), showing monodisperse pores for *MSN-A*, centered at 6.3 nm, while *MSN-B* has mesopores in the 3.5–9.0 nm range, with a maximum at 8.1 nm. *MSN-A* has higher specific surface area (787 m^2 g^{-1}) than *MSN-B* (755 m^2 g^{-1}) but lower total pore volume (1.27 versus 1.53 cm^3 g^{-1}).

Transmission electron microscopy (TEM) measurements were performed on the *MSN-A* sample in order to corroborate the XRD and N$_2$ porosimetry measurements. The pore diameter computed from TEM measurements is 6.1 nm, in very good agreement with porosimetry data. The interconnected, perpendicular mesochannels are also evidenced in the TEM images. The mesopore wall thickness was computed as 3.2 ± 0.4 nm from the TEM measurements. These pore diameter and wall thickness values are similar to other reported mesoporous silica with cubic ordered pore arrays, such as SBA-16 [22]. The measurements confirm that the mesoporous matrix has high porosity and interconnected pores, thus being able to adsorb the PCMs salts (Fig. 2).

Characterization of NaCl–CaCl$_2$ shape-stabilized PCMs

Samples containing between 70 and 95 mass% NaCl–CaCl$_2$ salt mixture were prepared (Table 1). Wide-angle XRD (Fig. 3a) was used to characterize the crystalline phases present in the composites. The diffraction patterns show the presence of both crystalline, anhydrous NaCl and CaCl$_2$ as well as several reflections belonging to calcium silica hydrate phases. The calcium silicate consists of tobermorite, $Ca_5Si_6O_{16}(OH)_2 \cdot 4H_2O$, a silica-rich phase which is stable toward dehydration at temperatures up to 750 °C [23]. Low-angle XRD shows the disappearance of the characteristic Bragg reflections belonging to the ordered mesophase (Fig. 3b). The lack of small-angle diffraction patterns can be explained by both the disappearance of the silica matrix through reaction with calcium

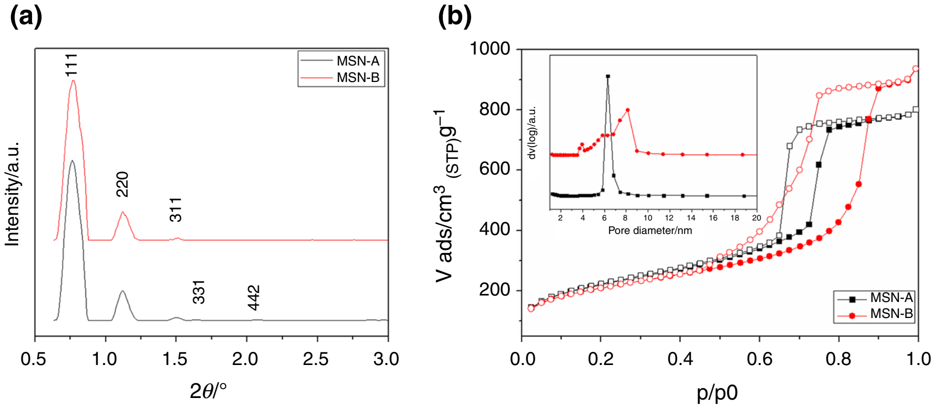

Fig. 1 Small-angle XRD with background subtracted (**a**) and N$_2$ adsorption–desorption isotherms (**b**) of the mesoporous matrices, with full and open symbols denoting the adsorption and desorption branches, respectively. Inset, the pore size distribution

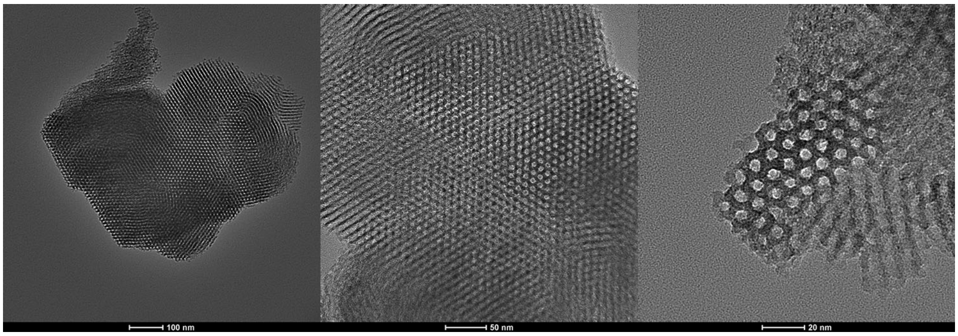

Fig. 2 TEM images of *MSN-A*

Table 1 Composite PCMs samples, salt mixture content, heat of fusion, melting points (m.p.) and crystallization temperature (c.t.) computed as onset temperatures and decomposition temperature (T_d), computed as the onset temperature of the DTG curve

Sample	NaCl–$CaCl_2$/mass%	ΔH/J g^{-1}	m.p./°C	c.t./°C	T_d/°C
70NaCl–$CaCl_2$/MSN-A	70	–	–		
80NaCl–$CaCl_2$/MSN-A	80	–	–		
90NaCl–$CaCl_2$/MSN-A	90	20.1	494.5	498.2	
95NaCl–$CaCl_2$/MSN-A	95	32.6	498.6	498.2	745
70NaCl–$CaCl_2$/MSN-B	70	–	–		
80NaCl–$CaCl_2$/MSN-B	80	–	–		
90NaCl–$CaCl_2$/MSN-B	90	25.6	498.7	499.9	751
95NaCl–$CaCl_2$/MSN-B	95	60.8	499.1	499.7	700
NaCl–$CaCl_2$	100	208.2	499.5		

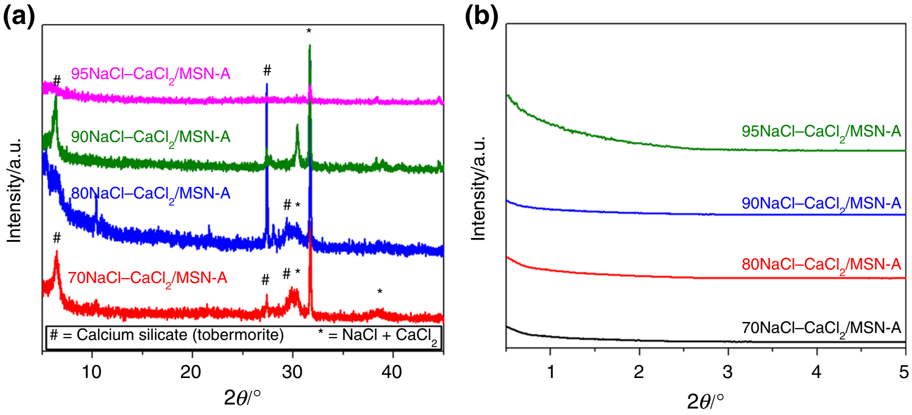

Fig. 3 Wide-angle (**a**) and low-angle (**b**) XRD patterns of representative composite samples

chloride and the filling of the remaining mesopores with the salt mixture.

FT-IR spectroscopy was carried out to assess the chemical composition of the composite PCMs in comparison with MSN and the pristine salt mixture. The spectrum of the MSN matrix presents the characteristic vibrations associated with asymmetric and symmetric Si–O–Si stretching at 1080 and 800 cm^{-1}; the Si–OH stretching vibrations at 960 cm^{-1} and Si–O–Si bending at 457 cm^{-1} [17, 24]. The wide bands at 3436 and 1630 cm^{-1} can be attributed to O–H vibrations of silanol groups and physisorbed water, respectively. The FT-IR spectra of composites containing 70% or 80% salt remain similar to the parent MSN spectrum (Fig. 4a). The SiO_2 network of *70NaCl–$CaCl_2$/MSN-A* and *80NaCl–$CaCl_2$/MSN-A* materials is depolymerized by interaction with salts as can be noticed from the supplementary bands at 1484 (1468) cm^{-1}; 990 (975) cm^{-1} appearing in their spectra. The wider band at 457 cm^{-1} and the asymmetric and symmetric Si–O–Si stretching bands are also shifted to lower wavenumbers (1050, 1039 cm^{-1}) by depolymerization. The band at 700 cm^{-1} can be assigned to bending motions of Si–O–Si bonds. This vibration overlaps with the wide band centered at 457 cm^{-1}. The number of bands in the range 650–750 cm^{-1} and the band at 906 cm^{-1} can be correlated with crystallization of silicates [25, 26].

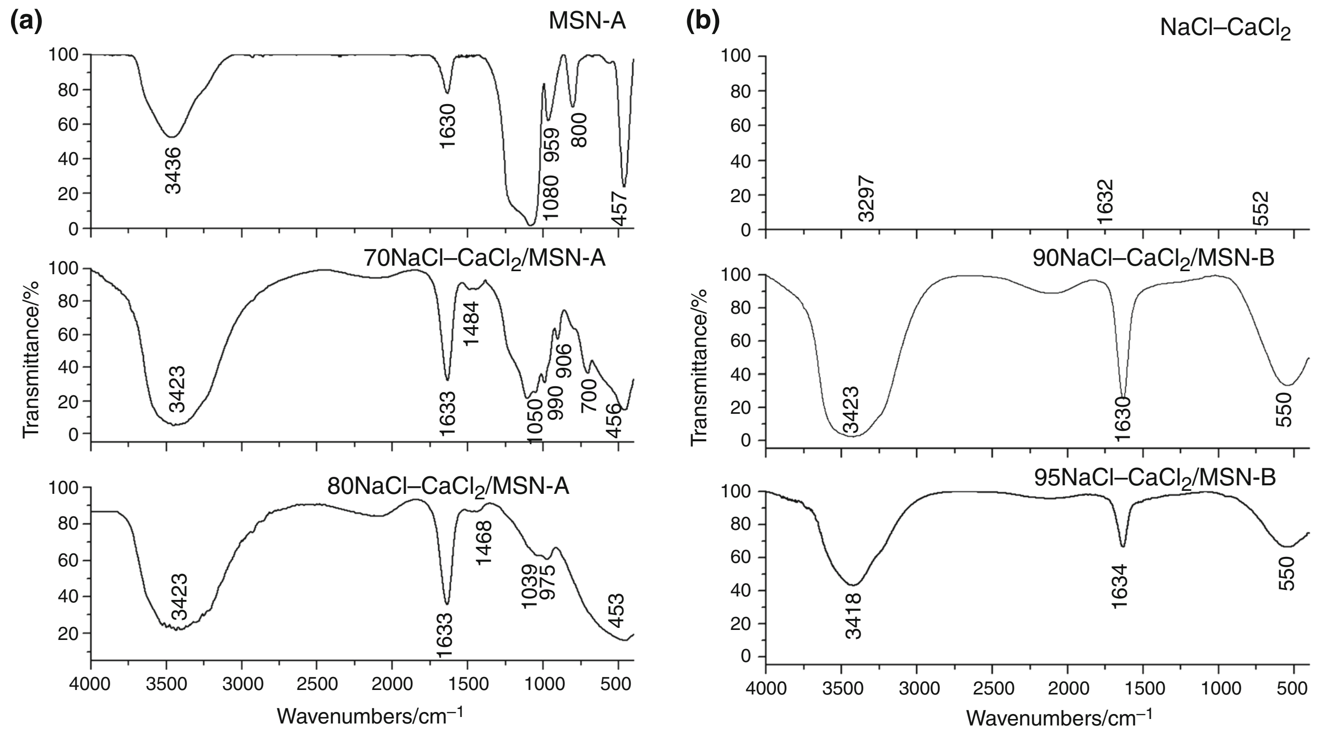

Fig. 4 Representative FT-IR spectra of the MSN matrix and low salt content composites (**a**) and chloride mixture and high salt content PCMs (**b**)

In contrast, the spectra of the composites containing 90% or 95% salt are similar to the spectrum of the pristine NaCl–CaCl$_2$ mixture (Fig. 4b). The specific vibrations of the mesoporous silica are absent, indicating its complete transformation into silicate. Since excess chloride mixture is required for the heat storage application, as this phase is the active latent heat phase, these materials could act as PCMs even after the transformation of the silica matrix into silicate.

Surface chemistry analysis by XPS was carried out to confirm the changes in the mesoporous silica matrix after impregnation and reaction with the chloride mixture. The most prominent transitions of the elements detected on the outermost surface layer (< 10 nm) were collected as high-resolution photoelectron spectra: Si2p, O1s, (Fig. 5) Na1s and Ca2p (Fig. S1, supplementary material). It is appropriate to notice that the experimental errors for the Binding Energies (BEs) assignments are within ± 0.2 eV. Figure 5 shows the Si2p and O1 XPS spectra of the MSN-B and *80NaCl–CaCl$_2$/MSN-B* samples. The Si2p detected at BE = 103.3 eV (a) and O1s BE = 533.2 eV (c) are attributed to the SiO$_2$ lattice for the *MSN-B* sample. The presence of new components can be noticed when comparing *80NaCl–CaCl$_2$/MSN-B* to the mesoporous silica matrix. The Si2p spectral deconvolution for *80NaCl–CaCl$_2$/MSN-B* shows that the sample contains 25.4% SiO$_2$ (BE = 103.3 eV) and 74.4% Ca$_x$SiO$_{2+x}$ (BE = 102.3 eV) (Fig. 5b).

On the other hand, the O1s deconvoluted spectrum (Fig. 5d) exhibits the presence of four components: oxygen bonded in the calcium silicate (30.8%, BE = 530.5 eV), hydroxyl groups adsorbed on the surface (44,9%, BE = ~ 532.0 eV), SiO$_2$ (14.7%, BE = 533. 2 eV) and the NaKLL Auger transition. Na was detected only as sodium bound in NaCl (see Fig. S1 A, B, supplementary material). The XPS analysis also revealed the presence of calcium silicate species. For the *80NaCl–CaCl$_2$/MSN-B* sample, a significant chemical shift was observed compared with CaCl$_2$ standard. The calcium silicate chemical specie detected on the surface was confirmed by the binding energy shifted slightly to lower value (~ 347 eV). It is worth to mention that the presence of the CaO cannot be completely ruled out. Thus, the XPS analyses highlight that the composite samples contain a mixture of calcium silicate and silica.

The morphology of the chloride composite was compared with that of the parent MSN through SEM analyses (Fig. 6). The mesoporous matrix is composed of roughly spherical particles, which form agglomerates. After the encapsulation and reaction with the molten chloride mixture, both spherical particles and lamellar phases can be noticed. The latter denotes the presence of the NaCl–CaCl$_2$ mixture while the former shows the preservation of the mesoporous silica particle shape after the silicate formation reaction. The morphology of the *90NaCl–CaCl$_2$/MSN-*

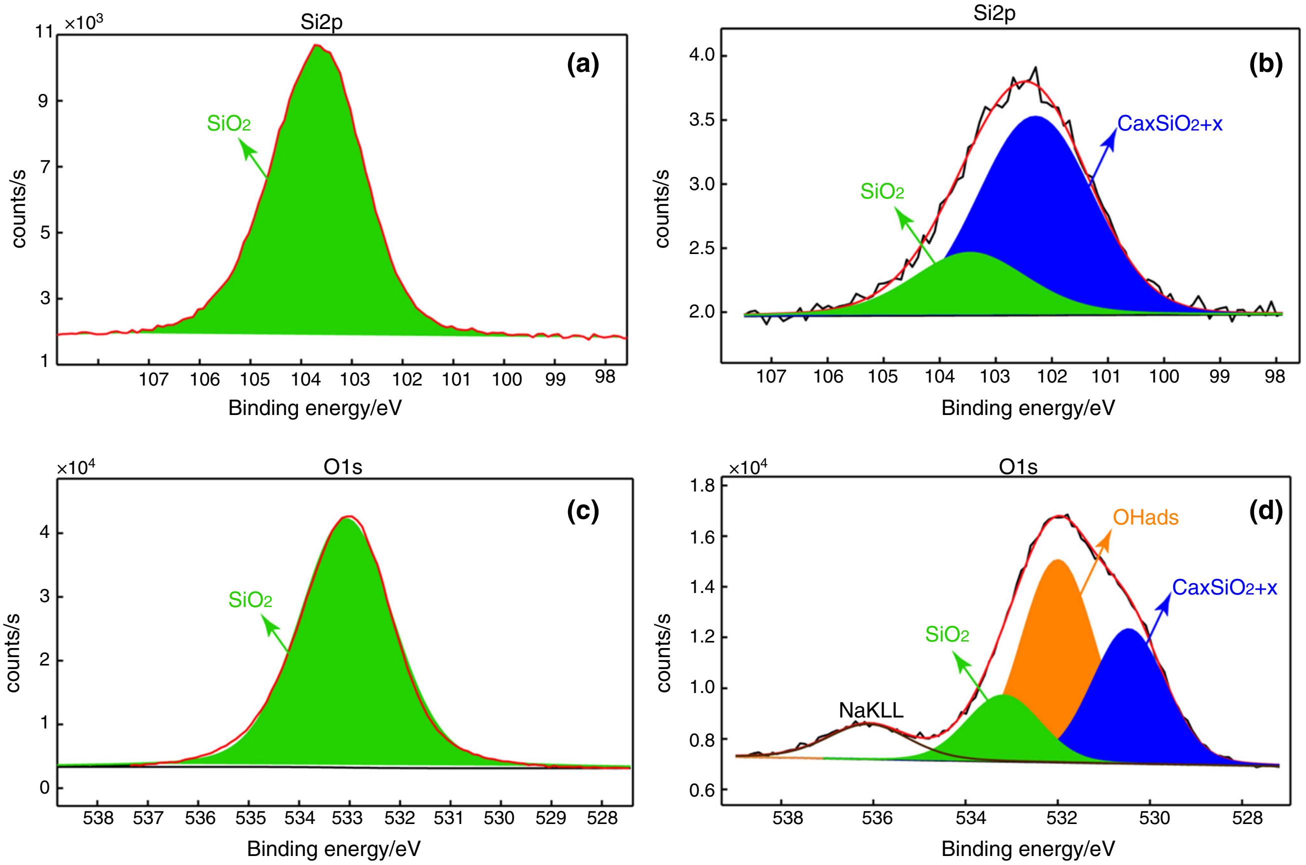

Fig. 5 Si2p and O1s deconvoluted photoelectron spectra for MSN-B and 80NaCl–$CaCl_2$/MSN-B

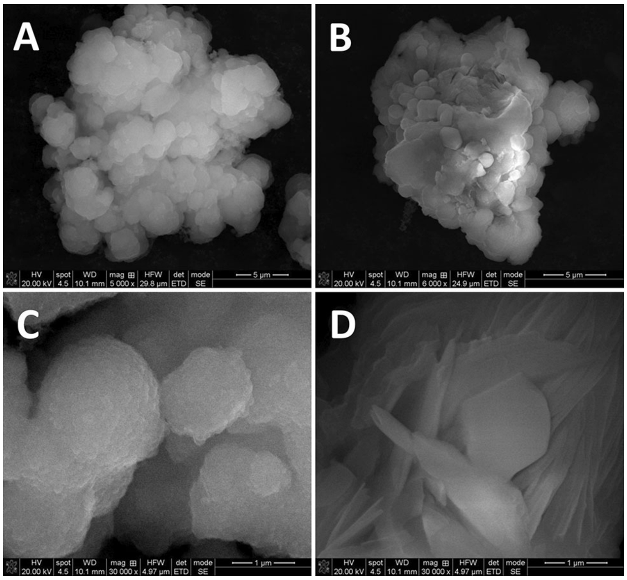

Fig. 6 SEM analyses of *MSN-B* (**a**, **c**) and *90NaCl–CaCl$_2$/MSN-B* (**b**, **d**)

B shows a good homogeneity of the chloride salts and silicate matrix (Fig. 6b, d).

Thermal properties of the composite PCMs and shape stability

DSC measurements were performed in order to assess the composites heat storage capacity and compared with the bulk NaCl–$CaCl_2$ mixture (Fig. 7). Melting points (m.p.) were determined as the onset temperature of the salt melting. The pristine salt has a melting point of 499.5 °C and heat of fusion of 208.2 J g^{-1}. Only the samples with 90% and 95 mass% salt show appreciable melting events (Fig. 7a). Interestingly, the melting points of the materials based on *MSN-A* are slightly reduced in comparison with the bulk salt: 494.5 and 498.6 °C for *90NaCl–CaCl$_2$/MSN-A* and *95NaCl–CaCl$_2$/MSN-A*, respectively. This melting point reduction is typically associated with the decrease in the size of the crystalline phase in nanoconfined materials [27]. The melting point decrease equals 5.0 and 0.9 °C for the 90% and 95% salt composites. It is worth noting that nanoconfinement in mesopores up to 40 nm in diameter is accompanied with decreases of 10–30 °C, while smaller differences are obtained for crystalline phases confined in the interparticle space [14]. It is likely that the melting point decrease for the *MSN-A*-based samples is caused by the salt confinement in the interparticle spaces. Composites

Fig. 7 DSC analyses of the composite PCMs on the heating (**a**) and cooling (**b**) runs. Heat flow was normalized to sample size; the DSC traces are shifted on the y-axis for clarity

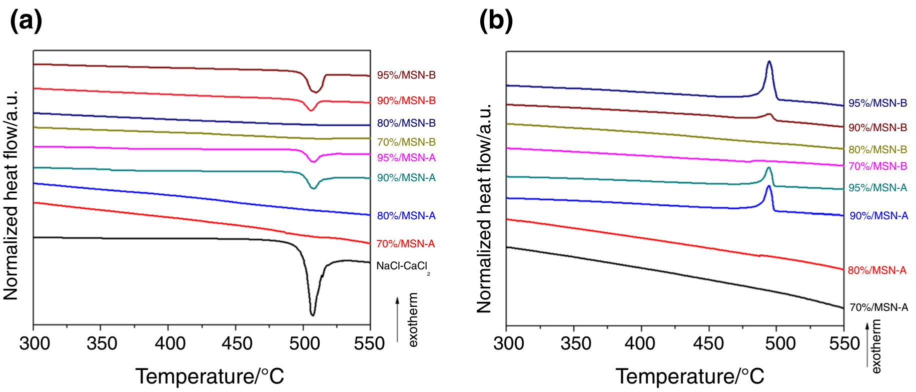

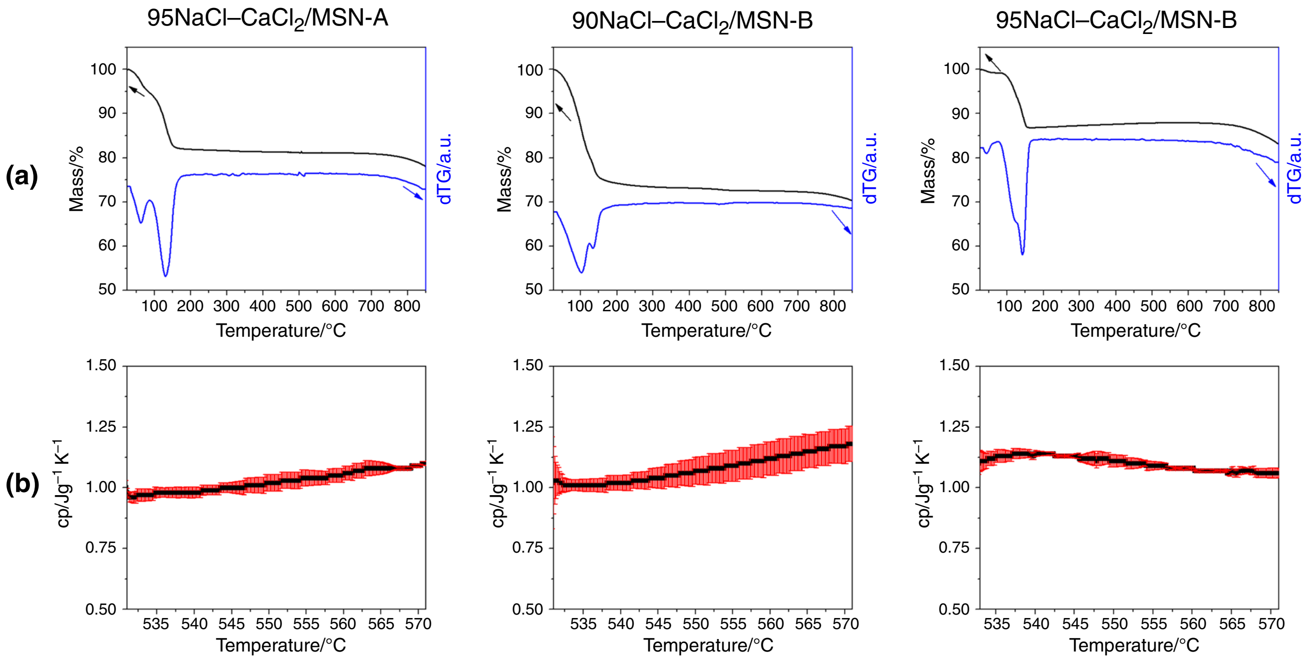

Fig. 8 Thermogravimetric analyses (**a**) and specific heat capacity measurements (**b**) for salt-mesoporous silica samples. The shaded red area in fig. B represents the c_p standard deviation (n = 3). (Color figure online)

obtained from *MSN-B* exhibit similar melting points with the chloride mixture (Table 1). The composite samples do not show supercooling, as the crystallization temperature is similar to the NaCl–CaCl$_2$ m.p. in all cases (Fig. 7b, Table 1).

The melting and crystallization enthalpy is one of the most important parameters for heat storage applications. The heat of fusion increases with increasing the salt content from 90% to 95%. The samples prepared with *MSN-A* have lower enthalpy values than the materials obtained from *MSN-B* at the same salt concentration. The highest heat of fusion value of 60.8 J g^{-1} was obtained for *95NaCl–CaCl$_2$/MSN-B*. Samples *95NaCl–CaCl$_2$/MSN-A* and *90NaCl–CaCl$_2$/MSN-B* also exhibit good enthalpy values, at 32.6 J g^{-1} and 25.6 J g^{-1}, respectively.

All enthalpy values are lower than the heat of fusion expected from the mass ratio of the salt mixture. This fact can be understood by taking into account the reaction between calcium chloride and the mesoporous silica matrix, evidenced by XRD, XPS and FT-IR measurements. The formation of the calcium silicate decreases the calcium chloride content. NaCl does not participate in the reaction, as evidenced by XPS analyses. Thus, the concentration of the NaCl–CaCl$_2$ eutectic is decreased with respect to the initial synthesis amount and the NaCl–CaCl$_2$ system has higher Na concentration than the eutectic composition. The consumption of calcium and silica species also account for the decrease and disappearance of the eutectic melting at lower salt concentrations. The samples containing 70% and 80% salt have molar Si/Ca ratio higher than or close to 1 and show the presence of unreacted silica in their FT-IR spectra.

Thermal stability and specific heat capacity influence the samples operating temperature range and sensible heat storage capacity, respectively. The NaCl–$CaCl_2$ mesoporous silica composites can combine latent and sensible heat storage. The 3 samples with the highest melting enthalpy, *95NaCl–*$CaCl_2$*/MSN-A*, *90NaCl–*$CaCl_2$*/MSN-B* and *95NaCl–*$CaCl_2$*/MSN-B* were selected for further study.

Thermogravimetric analyses (Fig. 8a) of the selected samples are characterized by two mass loss stages: a two-step mass loss from 50 to 150 °C associated with the loss of adsorbed water and the loss of chloride salts at temperatures above 700 °C. The decomposition temperature was computed as the onset of the salt loss, using the dTG curve. All samples are stable up to 700 °C. Interestingly, the decomposition temperature is inversely correlated with the heat of fusion values, which can be explained if the eutectic salt is lost through evaporation.

The specific heat capacity was recorded above the NaCl–$CaCl_2$ eutectic melting point and within the limits of our experimental setup. All 3 composite PCMs exhibit similar c_p values between 1.0 and 1.1 J g^{-1} K^{-1} (Fig. 8b). These values are comparable with other proposed PCMs for high-temperature energy storage, which are between 0.5 and 1.7 J g^{-1} K^{-1} [6]. The heat capacity of molten halide salts was shown not to vary with temperature and to have a constant value per mol of atoms in non-lithium and non-fluoride salts [28]. A theoretical heat capacity of 1.07 J g^{-1} K^{-1} can be computed for the NaCl–$CaCl_2$ mixture based on that observation, which agrees with the experimentally determined values.

Lastly, the propensity of the composites to retain their macroscopic shape after heating above the salt eutectic melting point was assessed (Fig. S2, supplementary material). No significant changes were noticed before and after heating, suggesting that the materials are shape-stabilized.

Conclusions

The synthesis of shape-stabilized phase change materials based on NaCl–$CaCl_2$ eutectic salt mixture and mesoporous silica was studied for the first time. Two mesoporous silica materials with cubic pore arrangement and average pore diameters of 6.3 and 8.1 nm were obtained and characterized. Shape-stabilized composites were synthesized with a total salt content between 70 and 95 mass%. Only samples with at least 90% salt exhibit melting and crystallization of the NaCl–$CaCl_2$ eutectic. The maximum heat of fusion of 60.8 J g^{-1} was obtained for the 95 mass% salt loading on the mesoporous silica with the largest pore diameter. The melting point and crystallization temperature are similar to the 499.5 °C m.p. of the pristine salt PCM. Specific heat capacities of 1.0–1.1 J g^{-1} K^{-1} were obtained at temperatures above the eutectic melting point.

The melting enthalpies are lower than expected solely from the mass fraction of the salt mixture. The decrease stems from a reaction between the calcium salt and silica matrix, yielding calcium silicates, which shifts the Na/Ca ratio from the eutectic composition. The mesoporous silica acts as a reactive matrix in the synthesis of NaCl–$CaCl_2$ composites. All composite samples show good thermal stability up to 700 °C. Materials based on mesoporous silica and sodium/calcium chlorides are therefore promising for high-temperature heat storage through combined latent and sensible storage mechanisms.

Acknowledgements The financial support of the Romanian project PN-III-P1-1.1-TE-2016-0520, No. 95/2018 is greatly appreciated. The authors are grateful to Dr. Cornel Munteanu for performing the TEM measurements.

References

1. Zhang G, Li J, Chen Y, Xiang H, Ma B, Xu Z, et al. Encapsulation of copper-based phase change materials for high temperature thermal energy storage. Sol Energy Mater Sol Cells. 2014;128:131–7. https://doi.org/10.1016/j.solmat.2014.05.012.
2. Kenisarin MM. High-temperature phase change materials for thermal energy storage. Renew Sustain Energy Rev. 2010;14(3):955–70. https://doi.org/10.1016/j.rser.2009.11.011.
3. Gil A, Medrano M, Martorell I, Lázaro A, Dolado P, Zalba B, et al. State of the art on high temperature thermal energy storage for power generation. Part 1—concepts, materials and modellization. Renew Sustain Energy Rev. 2010;14(1):31–55. https://doi.org/10.1016/j.rser.2009.07.035.
4. Zhang Q, Liu J. Nano liquid metal as an emerging functional material in energy management, conversion and storage. Nano Energy. 2013;2(5):863–72. https://doi.org/10.1016/j.nanoen.2013.03.002.
5. Schrader AJ, Muroyama AP, Loutzenhiser PG. Solar electricity via an air brayton cycle with an integrated two-step thermochemical cycle for heat storage based on Co_3O_4/CoO redox reactions: thermodynamic analysis. Sol Energy. 2015;118:485–95. https://doi.org/10.1016/j.solener.2015.05.045.
6. Liu M, Saman W, Bruno F. Review on storage materials and thermal performance enhancement techniques for high temperature phase change thermal storage systems. Renew Sustain Energy Rev. 2012;16(4):2118–32. https://doi.org/10.1016/j.rser.2012.01.020.
7. Wu S, Ma X, Peng D, Bi Y. The phase change property of lauric acid confined in carbon nanotubes as nano-encapsulated phase change materials. J Therm Anal Calorim. 2018. https://doi.org/10.1007/s10973-018-7906-3.
8. Mitran R-A, Berger D, Matei C. Improving thermal properties of shape-stabilized phase change materials containing lauric acid and mesocellular foam silica by assessing thermodynamic properties of the non-melting layer. Thermochim Acta. 2018;660:70–6. https://doi.org/10.1016/j.tca.2017.12.019.

9. Liu S, Ma G, Xie S, Jia Y, Sun J, Jing Y. Diverting the phase transition behaviour of adipic acid via mesoporous silica confinement. RSC Adv. 2016;6(113):111787–96. https://doi.org/10.1039/c6ra23498d.
10. Deng S, Wang D, Wang X, Wei Y, Waterhouse GI, Lan XZ. Effect of nanopore confinement on the thermal and structural properties of heneicosan. Thermochim Acta. 2018;664:57–63.
11. Tran N, Zhao W, Carlson F, Davidson JH, Stein A. Metal nanoparticle–carbon matrix composites with tunable melting temperature as phase-change materials for thermal energy storage. ACS Appl Nano Mater. 2018;1(4):1894–903.
12. Fernández AI, Barreneche C, Belusko M, Segarra M, Bruno F, Cabeza LF. Considerations for the use of metal alloys as phase change materials for high temperature applications. Sol Energy Mater Sol Cells. 2017;171:275–81. https://doi.org/10.1016/j.solmat.2017.06.054.
13. Aftab W, Huang X, Wu W, Liang Z, Mahmood A, Zou R. Nanoconfined phase change materials for thermal energy applications. Energy Environ Sci. 2018. https://doi.org/10.1039/c7ee03587j.
14. Mitran R-A, Berger D, Matei C. Phase change materials based on mesoporous silica. Curr Org Chem. 2018;22(27):2644–63. https://doi.org/10.2174/1385272822666180827125651.
15. Majda D, Korzeniowska A, Makowski W, Michalik-Zym A, Napruszewska BD, Zimowska M, et al. Thermoporosimetry of *n*-alkanes for characterization of mesoporous SBA-15 silicas—refinement of methodology. Microporous Mesoporous Mater. 2016;222:33–43. https://doi.org/10.1016/j.micromeso.2015.10.002.
16. Chen D, Chen Y, Guo X, Tao W, Wang J, Gao S, et al. Mesoporous silica nanoparticles with wrinkled structure as the matrix of myristic acid for the preparation of a promising new shape-stabilized phase change material via simple method. RSC Adv. 2018;8(60):34224–31. https://doi.org/10.1039/c8ra06536e.
17. Mitran R-A, Nastase S, Matei C, Berger D. Tailoring the dissolution rate enhancement of aminoglutethimide by functionalization of MCM-41 silica: a hydrogen bonding propensity approach. RSC Adv. 2015;5(4):2592–601. https://doi.org/10.1039/c4ra11224e.
18. Linares N, Silvestre-Albero AM, Serrano E, Silvestre-Albero J, Garcia-Martinez J. Mesoporous materials for clean energy technologies. Chem Soc Rev. 2014;43(22):7681–717. https://doi.org/10.1039/c3cs60435g.
19. Qian T, Li J, Min X, Deng Y, Guan W, Ning L. Radial-like mesoporous silica sphere: a promising new candidate of supporting material for storage of low-, middle-, and high-temperature heat. Energy. 2016;112:1074–83. https://doi.org/10.1016/j.energy.2016.07.023.
20. Mitran RA, Berger D, Munteanu C, Matei C. Evaluation of different mesoporous silica supports for energy storage in shape-stabilized phase change materials with dual thermal responses. J Phys Chem C. 2015;119(27):15177–84. https://doi.org/10.1021/acs.jpcc.5b02608.
21. Fan J, Yu C, Gao F, Lei J, Tian B, Wang L, et al. Cubic mesoporous silica with large controllable entrance sizes and advanced adsorption properties. Angew Chem. 2003;115(27):3254–8. https://doi.org/10.1002/ange.200351027.
22. Grudzien RM, Grabicka BE, Jaroniec M. Adsorption studies of thermal stability of SBA-16 mesoporous silicas. Appl Surf Sci. 2007;253(13):5660–5. https://doi.org/10.1016/j.apsusc.2006.12.033.
23. Palubinskaitė D, Kantautas A. Influence of tribomechanical milling and activation of primary mixtures on the synthesis of calcium silicate hydrates. Mater Sci Poland. 2006;24(2/1):396–403.
24. Mocioiu OC, Mocioiu A-M, Marin A, Zaharescu M. Study of historical lead silicate glasses and their preservation by silica coating. Ceram Int. 2017;43(1):77–83. https://doi.org/10.1016/j.ceramint.2016.09.055.
25. Zaharescu M, Mocioiu OC, Andronescu C. Influence of CaO addition on the structure and properties of the glasses in the SiO$_2$–PbO–Na$_2$O system. J Optoelectron Adv Mater. 2008;10(6):1315–9.
26. Yu P, Kirkpatrick RJ, Poe B, McMillan PF, Cong X. Structure of calcium silicate hydrate (C–S–H): near-, mid-, and far-infrared spectroscopy. J Am Ceram Soc. 1999;82(3):742–8. https://doi.org/10.1111/j.1151-2916.1999.tb01826.x.
27. Hugo KC. Confinement effects on freezing and melting. J Phys: Condens Matter. 2001;13(11):R95.
28. Redkin AA, Zaikov YP, Korzun IV, Reznitskikh OG, Yaroslavtseva TV, Kumkov SI. Heat capacity of molten halides. J Phys Chem B. 2015;119(2):509–12. https://doi.org/10.1021/jp509932e.